Extended law of corresponding states: square-well oblates

Miguel Gómez de Santiago
Área de Física de Procesos Irreversibles, División de Ciencias Básicas e Ingeniería, Universidad Autónoma Metropolitana-Azcapotzalco, Av. San Pablo 180, 02200 Ciudad de México, Mexico

Péter Gurin
Physics Department, Center for Natural Sciences, Faculty of Engineering, University of Pannonia, P.O.Box 158, Veszprém H-8201, Hungary

Szabolcs Varga
Physics Department, Center for Natural Sciences, Faculty of Engineering, University of Pannonia, P.O.Box 158, Veszprém H-8201, Hungary

Gerardo Odriozola
Área de Física de Procesos Irreversibles, División de Ciencias Básicas e Ingeniería, Universidad Autónoma Metropolitana-Azcapotzalco, Av. San Pablo 180, 02200 Ciudad de México, Mexico

E-mail: `godriozo@azc.uam.mx`

Abstract. The vapour-liquid coexistence collapse in the reduced temperature, $T_r = T/T_c$, reduced density, $\rho_r = \rho/\rho_c$, plane is known as a principle of corresponding states, and Noro and Frenkel have extended it for pair potentials of variable range. Here, we provide a theoretical basis supporting this extension, and show that it can also be applied to short-range pair potentials where both repulsive and attractive parts can be anisotropic. We observe that the binodals of oblate hard ellipsoids for a given aspect ratio ($\kappa = 1/3$) with varying short-range square-well interactions collapse into a single master curve in the ΔB_2^*–ρ_r plane, where $\Delta B_2^* = (B_2(T) - B_2(T_c))/v_0$, B_2 is the second virial coefficient, and v_0 is the volume of the hard body. This finding is confirmed by both REMC simulation and second virial perturbation theory for varying square-well shells, mimicking uniform, equator, and pole attractions. Our simulation results reveal that the extended law of corresponding states is not related to the local structure of the fluid.

1. Introduction

It is well-known that the reduced form of the van der Waals equation of states is independent of the substance. Thus, two different substances sharing a couple of reduced thermodynamic variables are said to be in correspondence, since they approximately yield all same reduced properties. The principle can be expressed as $P_r = u(T_r, V_r)$, where $P_r = P/P_c$, $T_r = T/T_c$, and $V_r = V/V_c$ are the reduced pressure, temperature, and volume, respectively, and where the subindexes r and c stand for reduced and critical. Here, u is some universal function. Due to the Gibbs phase rule, the principle may take the form $T_r = w(\eta_r)$ for any two-phase coexistence, where $\eta_r = \eta/\eta_c$, $\eta = Nv_0/V$ is the packing fraction, N is the number of particles contained in the system, and v_0 is the volume of the particle core.

Although the principle works very well for describing the liquid-vapor coexistence of monoatomic substances, such as Neon, Argon, and Krypton, and several diatomic molecules, such as Nitrogen and Oxygen among others [1], it generally yields poor results for very anisotropic molecules and colloids. On one hand, the pair potential turns angular dependent, and on the other hand, its range strongly depends on particle and solvent properties [2]. Note that colloids may show tiny attraction ranges when compared with their core size. This fact encouraged Noro and Frenkel to propose an extension of this corresponding principle [3] with application to colloids and protein solutions [4, 5, 6, 7, 8, 9].

Their idea was to replace T_r with a better measure of the attraction in terms of the particle excluded volume. This way, one should be able to account for different attraction ranges and depths. They propose the reduced second virial coefficient, $B_2(T^*)/B_2^{HS}$, where $B_2^{\mathrm{HS}} = 2\pi\sigma^3/3$ is the second virial coefficient of hard-spheres ($T^* = k_BT/\epsilon$, ϵ being the depth of the pair-potential and k_B the Boltzmann constant), as a replacement of T_r. Taking the square-well potential [10, 11, 12, 13, 14, 15, 16], for instance, $B_2(T^*)/B_2^{HS}$ remains the same when scaling the particle size and the attraction range, or when varying the range of the attractive shell while compensating this variation with the well-depth. Thus, different attraction ranges may result in the same $B_2(T^*)/B_2^{HS}$ for the same hardcore.

Noro and Frenkel [3] give a further step by assuming $B_2(T_c^*)/B_2^{HS} \approx -1.5$, where $T_c^* = k_BT_c/\epsilon$. This is a very convenient proposal since, given a particular pair potential, T_c^* would be fully determined. Adding to this knowledge the shape of the master curve, $B_2(T^*)/B_2^{HS}$, one would determine the reduced density, η_r, at any T^*. Unfortunately, $B_2(T_c^*)/B_2^{HS} \approx -1.5$ is not always a good approximation [17, 18, 19, 16, 20, 21, 22] and introduces a shift (up or down) of the $B_2(T^*)/B_2^{HS}$ curves, making them to poorly collapse, even for spherically symmetric pair potentials [21]. Thus, we suggested to undo this last step and employ $\Delta B_2^*(T^*) = (B_2(T^*) - B_2(T_c^*))/v_0$ instead [21].

At the level of the second virial perturbation, we first demonstrate that the liquid-vapor coexistence in the $\Delta B_2^*(T^*)$-η_r plane yields a single master curve for all attractive shells and hardcores of a given size and shape, as shown in the following section.

Since this does not guarantee the fulfillment of the corresponding states principle for short-range potentials, we then focus on a particular system of attractive anisotropic particles [23, 4, 24, 25, 26, 27]. That is, we studied the short-range behavior of oblates having a fixed anisotropy but variable square-well shapes and ranges for the attractive contribution. In particular, we explore what we have called homogenous, equator, and pole attraction. The details of the model are given in section 3. Section 4 briefly exposes our replica-exchange Monte Carlo (REMC) implementation aimed to solve the liquid-vapor coexistence. Finally, results are shown in section 5. Here, as predicted by the theory, we observe these different attraction shells to yield liquid-vapor coexistence data falling in the same master curve when depicted in the $\Delta B_2^*(T^*)$-η_r plane. Conclusions are drawn at the end of this work in section 6.

2. Theory

Let us consider a very general model consisting of a hardcore repulsion surrounded by an attractive potential, each being anisotropic and having arbitrary shapes. The dimensionless free energy per particle, $f = \beta F/N$, of a macroscopic system made up of these entities is

$$f(\eta, T^*) = f_{\mathrm{HC}}(\eta) + f_{\mathrm{att}}(\eta, T^*) \simeq f_{\mathrm{HC}}(\eta) + \frac{\eta}{v_0} B_2^{\mathrm{att}}(T^*)\,, \tag{1}$$

where f_{HC} and f_{att} are the *exact* free energy of the hardcore repulsion and that of the attractive interaction, respectively, v_0 is the volume of the hardcore, η is the packing fraction, therefore η/v_0 is the number density, and $B_2^{\mathrm{att}}(T^*)$ is the second virial coefficient of the attractive part of the pair potential. Note that f_{att} is approximated on the level of second virial theory in Eq.(1) [28]. For anisotropic hard bodies, the second virial coefficient (in the isotropic phase) is $B_2(T^*) = -\frac{1}{2}\int \frac{d^2\omega_1}{4\pi}\frac{d^2\omega_2}{4\pi}\int d^3r\, f_M(\boldsymbol{r}, \hat{\boldsymbol{\omega}}_1, \hat{\boldsymbol{\omega}}_2)$, where $f_M(\boldsymbol{r}, \hat{\boldsymbol{\omega}}_1, \hat{\boldsymbol{\omega}}_2) = e^{-u(\boldsymbol{r}, \hat{\boldsymbol{\omega}}_1, \hat{\boldsymbol{\omega}}_2)/(\epsilon T^*)} - 1$ is the Mayer function, $u(\boldsymbol{r}, \hat{\boldsymbol{\omega}}_1, \hat{\boldsymbol{\omega}}_2)$ is the interparticle potential, $\boldsymbol{r} = \boldsymbol{r}_1 - \boldsymbol{r}_2$ is the center-to-center vector between the particles, and $\hat{\boldsymbol{\omega}}_i$ is their orientation unit vector. Due to the hard body nature of the repulsion, B_2 can be separated into two contributions, $B_2 = B_2^{\mathrm{HC}} + B_2^{\mathrm{att}}$, corresponding to the division of the space into two regions, where the particles do overlap, $\boldsymbol{r} \in \mathcal{V}_{\mathrm{ex}}(\hat{\boldsymbol{\omega}}_1, \hat{\boldsymbol{\omega}}_2)$, and do not, $\boldsymbol{r} \notin \mathcal{V}_{\mathrm{ex}}(\hat{\boldsymbol{\omega}}_1, \hat{\boldsymbol{\omega}}_2)$, respectively. That is, $B_2^{\mathrm{HC}} = -\frac{1}{2}\int \frac{d^2\omega_1}{4\pi}\frac{d^2\omega_2}{4\pi}\int_{\boldsymbol{r}\in\mathcal{V}_{\mathrm{ex}}} d^3r\, f_M(\boldsymbol{r}, \hat{\boldsymbol{\omega}}_1, \hat{\boldsymbol{\omega}}_2)$ and $B_2^{\mathrm{att}} = -\frac{1}{2}\int \frac{d^2\omega_1}{4\pi}\frac{d^2\omega_2}{4\pi}\int_{\boldsymbol{r}\notin\mathcal{V}_{\mathrm{ex}}} d^3r\, f_M(\boldsymbol{r}, \hat{\boldsymbol{\omega}}_1, \hat{\boldsymbol{\omega}}_2)$.

The model described through the free energy given by Eq.(1) has two key features. First, f_{HC} depends only on the density but not on the temperature. Second, the attraction is taken into account as a perturbation at the second virial level, despite the exact treatment of the hardcore repulsion. Consequently, the dimensionless temperature, T^*, and all the details of the attractive part of the potential appear together via $B_2^{\mathrm{att}}(T^*)$. Hence, it is possible to derive a master curve for the liquid-vapor coexistence, as shown in the following lines. Note that this treatment holds for any shape of the core and the shell of the attractive potential.

Via the thermodynamic relations $p = -\frac{\partial F}{\partial V}$ and $F = -pV + \mu N$, and the free energy given by Eq.(1), it follows the dimensionless pressure,

$$\beta p v_0 = \eta^2 \frac{\partial f}{\partial \eta} = \eta^2 f'_{\mathrm{HC}}(\eta) + \eta^2 B_2^{\mathrm{att}*}(T^*)\,, \tag{2}$$

and chemical potential,

$$\beta \mu = f + \frac{\beta p v_0}{\eta} = f_{\mathrm{HC}}(\eta) + \eta f'_{\mathrm{HC}}(\eta) + 2\eta B_2^{\mathrm{att}*}(T^*)\,, \tag{3}$$

where we used the notation $B_2^{\mathrm{att}*} = B_2^{\mathrm{att}}/v_0$ for the dimensionless second virial coefficient. At a given temperature, the liquid-vapor equilibrium densities, η_{v} and η_{l} can be determined via the mechanical and chemical equilibrium conditions $p(\eta_{\mathrm{v}}, T^*) = p(\eta_{\mathrm{l}}, T^*)$ and $\mu(\eta_{\mathrm{v}}, T^*) = \mu(\eta_{\mathrm{l}}, T^*)$, which reduce to

$$h_p(\eta_{\mathrm{v}}, \eta_{\mathrm{l}}) = B_2^{\mathrm{att}*}(T^*) \tag{4}$$

and

$$h_\mu(\eta_{\mathrm{v}}, \eta_{\mathrm{l}}) = B_2^{\mathrm{att}*}(T^*)\,, \tag{5}$$

where

$$h_p(\eta_{\mathrm{v}}, \eta_{\mathrm{l}}) = \frac{\eta_{\mathrm{v}}^2 f'_{\mathrm{HC}}(\eta_{\mathrm{v}}) - \eta_{\mathrm{l}}^2 f'_{\mathrm{HC}}(\eta_{\mathrm{l}})}{\eta_{\mathrm{l}}^2 - \eta_{\mathrm{v}}^2} \tag{6}$$

and

$$h_\mu(\eta_{\mathrm{v}}, \eta_{\mathrm{l}}) = \frac{f_{\mathrm{HC}}(\eta_{\mathrm{v}}) - f_{\mathrm{HC}}(\eta_{\mathrm{l}}) + \eta_{\mathrm{v}} f'_{\mathrm{HC}}(\eta_{\mathrm{v}}) - \eta_{\mathrm{l}} f'_{\mathrm{HC}}(\eta_{\mathrm{l}})}{2(\eta_{\mathrm{l}} - \eta_{\mathrm{v}})}\,. \tag{7}$$

The functions h_p and h_μ depend neither on the temperature nor the details of the attractive potential. Therefore, for a given $B_2^{\mathrm{att}*}(T^*)$ value, Eqs.(4)-(5) yield the same solution for the phase equilibrium densities for models having different attractive shapes, attractive ranges, and temperatures. In other words, in the $B_2^{\mathrm{att}*}$-η plane, the binodal curve is the same for all models having the same hardcore repulsion at the level of the attractive approximation.

From a practical point of view, the second virial of the whole model is a more natural quantity than that of the isolated attractive part. Thus, in the literature [21], there are representations of the so-called reduced and shifted second virial coefficient, $\Delta B_2^*(T^*) = (B_2(T^*) - B_2(T_c^*))/v_0$, against $\eta_r = \eta/\eta_c$, where T_c^* and η_c are the critical temperature and packing fraction, respectively, yielding quite nice master curves. The quantity $\Delta B_2^*(T^*)$ is actually a constant shift of $B_2^{\mathrm{att}*}$, as $\Delta B_2^*(T^*) = B_2^{\mathrm{att}*}(T^*) - B_2^{\mathrm{att}*}(T_c^*)$, because the hard body contribution of the second virial is independent of the temperature. Furthermore, at the level of our approximation, neither η_c nor $B_2^{\mathrm{att}*}(T_c^*)$ depend on the attractive part of the pair potential. Note that there is no gain on employing η_r as the independent variable instead of η. Nonetheless, there is no harm in using η_r as it is custom.

The reason for the existence of a master curve is the fact that the details of the attractive interaction, which is responsible for the vapour-liquid transition, is concentrated into $B_2^{\mathrm{att}*}$. This is a direct consequence of dealing with a hardcore repulsion

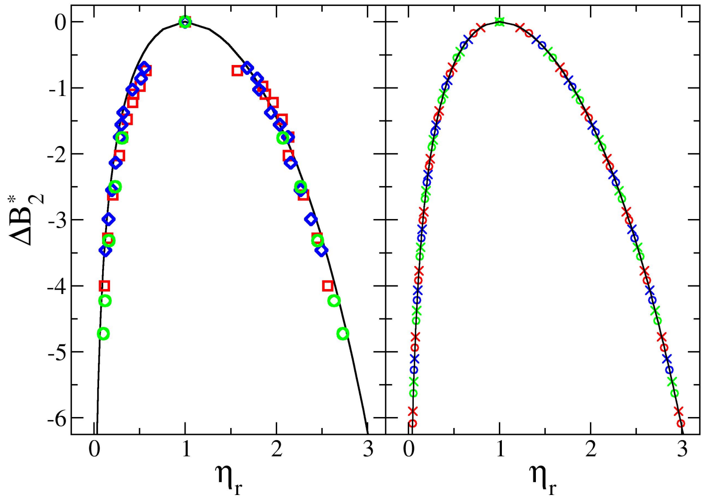

Figure 1. (left) Phase diagram for the outcomes of the theory for the spherical square-well model (the aspect ratio, κ, in this case is one). Red squares, green circles, and blue diamonds corresponds to simulations of the square-well potential for $\lambda = 1$, 1.3, and 1.5, as taken from references [29, 30]. (right) Phase diagram of the perturbation theory for attractive hard ellipsoids with an aspect ratio $\kappa = 1/3$. Crosses denote short-range attraction, $\lambda = 0.25$, while circles correspond to long-range cases, $\lambda = 5$. Red, blue, and green symbols depict uniform, equator, and pole attractions. The black line simply joins all the data.

plus an attractive term on the level of a second virial perturbation theory. Therefore, our perturbation theory is expected to be quite good for long-range but not so good for short-range attraction [13].

These theoretical findings encourage us to compare the theory outcomes with those from simulations. In particular, there are plenty simulations in the literature dealing with the square-well potential [29, 30, 31, 32, 18]. Although the core shape of the square-well is spherically symmetric, it also fulfills Eq.(1). As shown elsewhere [21], there is a marked jump from short to long-range behavior at $\lambda \lesssim 1$, λ being the width of the attractive shell measured from the particle's surface in units of the particle's diameter (see the formal definition in section 3). Note that this definition is sometimes different in the literature, where λ is measured from the particle's center. For $\lambda < 1$ and $\lambda \geq 1$, the $\Delta B_2^*(\eta_r)$ curves group defining two different master curves. The left panel of Fig. 1 shows some data from the second group, that is for $\lambda = 1$, 1.3, and 1.5, as red squares, green circles, and blue diamonds, respectively, which are compared to the theoretical results (see the solid curve in the figure). In this case, we employ the accurate Carnahan-Starling expression for the hard sphere contribution of the free energy. In addition, we use the non-spherical attractive square-well potential, which depends on the orientations of the particles. One can show that $B_2^{\mathrm{att}*}$ can be obtained from

$$B_2^{\mathrm{att}*}(T^*) = \frac{1}{2}(1 - e^{1/T^*})\frac{\langle V_{\mathrm{exc}}^{\mathrm{SW}}\rangle - \langle V_{\mathrm{exc}}^{\mathrm{HC}}\rangle}{v_0}\,, \tag{8}$$

where $\langle V_{\mathrm{exc}}^{\mathrm{X}}\rangle = \frac{1}{\pi}\int_0^\pi V_{\mathrm{exc}}^{\mathrm{X}}(\theta)\sin(\theta)d\theta$ are the orientational average of excluded volumes of the hard body (X=HC) and the attractive regions (X=SW), respectively. Note that θ is the angle between the orientations of particles 1 and 2, which is given by $\cos(\theta) = \hat{\boldsymbol{\omega}}_1 \cdot \hat{\boldsymbol{\omega}}_2$. In the left panel of Fig. 1, we use a spherical particle shape, which is surrounded by a spherical shell. As can be seen, the agreement between simulation results and the theoretical outcomes is very good. On the one hand, all simulation data defines a master curve as predicted by the theory. On the other, theory and simulation produce the same master curve, pointing out the quantitative correctness of the theory for long-range attractive wells, at least for the spherically symmetric case.

The right hand panel of Fig. 1 shows the theoretical results obtained when considering ellipsoidal hard particles surrounded by an ellipsoidal square-well potential. The details of the ellipsoidal model are given in the following section. In this case, we use the Parsons-Lee scaling approximation for the hard core contribution of the free energy

$$f_{\mathrm{HC}} = \log\eta - 1 + \frac{4\eta - 3\eta^2}{(1-\eta)^2}\frac{\langle V_{\mathrm{exc}}^{\mathrm{HC}}\rangle}{8v_0}, \tag{9}$$

where the factor $\langle V_{\mathrm{exc}}^{\mathrm{HC}}\rangle/8v_0$ accounts for the anisotropy of the ellipsoid. Although this is only a rough approximation, it is enough to show that the liquid-vapor phase diagram is indeed independent of the shape of the attractive part of the potential, the well-depth, or equivalently, the temperature, and the potential range, λ. Fig. 2 schematizes the cases considered in this work. As shown, the model takes into account an oblate hardcore embedded by an attractive shell ellipsoid, both sharing the same geometrical center and axis of revolution. We focus on uniform, equator, and pole attractive square-well shells. These cases are depicted by red, green, and blue symbols in the right panel of Fig. 1. Also, we employed crosses and circles to distinguish the short and long-range cases. As can be seen, all data perfectly fall in the same curve

It is worth mentioning that, for the long-range cases, we expect the usual power-law behavior near the critical point with a mean-field critical exponent, 1/2. Note also that the renormalization group (RG) theory can explain not only the power-law behavior near the critical point with a universal exponent, but based on its non-linearized version [33], it is also possible to obtain a mathematical expression for the liquid-vapor coexistence curve [34]. According to this theory, long-range and short-range potentials show different critical exponents, and for this reason alone, the master curve cannot be the same if it exists at all. In addition, the RG theory cannot explain the existence of a master curve away from the critical point. Therefore, the predictions of the above theory for the short-range cases are at least questionable and so, we should check them through MC simulations. From here on, we restrict our study to the uniform, equator, and pole cases depicted in Fig. 2.

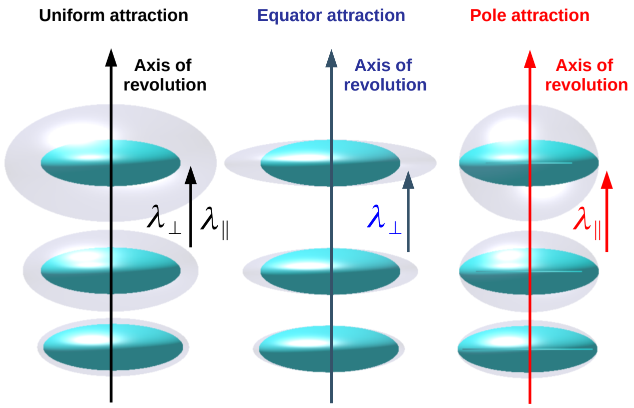

Figure 2. Oblates of increasing attraction range, λ, from bottom to top, having uniform (left), equator (middle), and pole (right) square-well attraction. The hardcore of the ellipsoids is solid cyan, whereas the attractive interaction is depicted as a glassy region surrounding the particles. In all cases, the hardcore aspect ratio is fixed, $\kappa = 1/3$. For uniform, equator, and pole attraction we define $\lambda = \lambda_\parallel = \lambda_\perp$, $\lambda = \lambda_\perp$ with $\lambda_\parallel = 0$, and $\lambda = \lambda_\parallel$ with $\lambda_\perp = 0$, respectively.

3. Model

The straightforward generalization of the square-well potential to ellipsoidal particles is given by [35]

$$u(r) = \begin{cases} \infty, & \text{for } r \leq \sigma_{\mathrm{i}}, \\ -\epsilon, & \text{for } \sigma_{\mathrm{i}} < r \leq \sigma_{\mathrm{o}}, \\ 0, & \text{for } \sigma_{\mathrm{o}} < r, \end{cases} \tag{10}$$

where r is the center-to-center distance, $\sigma_{\mathrm{i/o}}$ are the distances between the geometric centers of the inner (i) and outer (o) ellipsoids for ellipsoids at contact, and ϵ is the well depth. Contrasting with the usual square-well model, here $\sigma_{\mathrm{i/o}}$ depend on the particles' orientations and the shapes of the ellipsoids. We restrict this model to inner and outer ellipsoids sharing the same axis of revolution and the same geometrical center. Additionally, we further restrict the cases in this study to inner oblates. Thus, we have $\sigma_{\parallel,\mathrm{i}} \leq \sigma_{\perp,\mathrm{i}}$, where the equal sign is kept to consider spherical particles. We take the shortest principal axis, $\sigma_{\parallel,\mathrm{i}}$, as the unit of length. We also define $\kappa \equiv \sigma_{\parallel,\mathrm{i}}/\sigma_{\perp,\mathrm{i}}$ as the aspect ratio of the ellipsoids. Finally, we also restrict this study to $\kappa = 1/3$.

To approach the ellipsoidal shape for both inner and outer ellipsoids, we employ a modification of the Berne and Pechukas [36] closest approach distance, introduced by Rickayzen [37]. This modification fixes the T-shape mismatch while improving the approach to the exact solution and being analytically solvable [38]. The expression is given by

$$\sigma_{\mathrm{i/o}} = \frac{\sigma_{\perp,\mathrm{i/o}}}{\sqrt{1 - \frac{1}{2}\chi_{\mathrm{i/o}}[A^{+}_{\mathrm{i/o}} + A^{-}_{\mathrm{i/o}}] + (1-\chi_{\mathrm{i/o}})\chi'_{\mathrm{i/o}}[A^{+}_{\mathrm{i/o}}A^{-}_{\mathrm{i/o}}]^{\gamma}}}, \tag{11}$$

with

$$A^{\pm}_{\mathrm{i/o}} = \frac{(\hat{\mathbf{r}}\cdot\hat{\boldsymbol{\omega}}_1 \pm \hat{\mathbf{r}}\cdot\hat{\boldsymbol{\omega}}_2)^2}{1 \pm \chi_{\mathrm{i/o}}\,\hat{\boldsymbol{\omega}}_1\cdot\hat{\boldsymbol{\omega}}_2}, \tag{12}$$

$$\chi_{\mathrm{i/o}} = \frac{\sigma^2_{\parallel,\mathrm{i/o}} - \sigma^2_{\perp,\mathrm{i/o}}}{\sigma^2_{\parallel,\mathrm{i/o}} + \sigma^2_{\perp,\mathrm{i/o}}}, \tag{13}$$

and

$$\chi'_{\mathrm{i/o}} = \left(\frac{\sigma_{\parallel,\mathrm{i/o}} - \sigma_{\perp,\mathrm{i/o}}}{\sigma_{\parallel,\mathrm{i/o}} + \sigma_{\perp,\mathrm{i/o}}}\right)^2. \tag{14}$$

As mentioned, the inner and the outer ellipsoids share the same axis of revolution (see Fig. 2). In addition, $\hat{\mathbf{r}}$ is the unit vector along the line containing the ellipsoids' geometric centers, and γ is a parameter given in reference [38] to further approach the exact ellipsoidal contact distance.

In addition to κ, the hardcore aspect ratio, we define $\lambda_{\parallel} = \sigma_{\parallel,\mathrm{o}} - \sigma_{\parallel,\mathrm{i}}$ and $\lambda_{\perp} = \sigma_{\perp,\mathrm{o}} - \sigma_{\perp,\mathrm{i}}$ to parameterize the attraction range along the two main directions. For short, we refer to λ as the attraction range irrespective of the case. As mentioned, Fig. 2 schematizes some of the several possibilities of this model for inner oblates and with $\kappa = 1/3$. In particular, we focus on uniform attraction ($\lambda_{\parallel} = \lambda_{\perp}$) (left panel of Fig. 2), equator attraction ($\lambda_{\parallel} = 0$ and $\lambda_{\perp} > 0$) (middle panel of Fig. 2), and pole attraction ($\lambda_{\parallel} > 0$ and $\lambda_{\perp} = 0$) (right panel of Fig. 2). We have previously studied slightly different models for the uniform case, where we have focused on their inherent tendency to produce empty liquids for increasing anisotropy [26, 24, 25]. Empty liquids are typically yielded by low-valence fluids [39, 40, 41, 42, 43, 44] such as clays [45, 46, 47, 48, 43], protein isolates [49], and other type of colloids [43]. Here we deal with the possibility of defining a master curve for the liquid-vapor coexistence with $\kappa = 1/3$. For this purpose, we vary the attraction range, λ, from 0.25 to 1.5 in units of $\sigma_{\parallel}$ for equator and pole attraction, and from 0.25 to 1.0 for uniform attraction.

4. Simulation details

We employ the replica-exchange Monte Carlo (REMC) method [50, 51, 52] to obtain the liquid-vapor coexistence densities as a function of temperature for the square-well ellipsoids. A single run considers $M = 10$ square-based prismatic simulation cells containing a liquid slab at their center and vapor at each side [53]. The method sets different temperatures for each replica while including swap trial moves. These trials allow the replicas to sample from an expanded ensemble. This way, replicas at high temperatures travel long distances in configuration space, improving the sampling of the whole expanded ensemble. The definition of the extended ensemble is simply the product of the Canonical partition functions of each ensemble, Q_{NVT_i}, having N particles, volume V, and temperature T_i. That is, $Q_{\mathrm{ext}} = \prod_{\mathrm{i}=1}^{M} Q_{NVT_i}$. It is customary to fix the number of replicas, M, to the number of different ensembles so that each ensemble is sampled only by a single replica at a time. By forcing the detailed balance

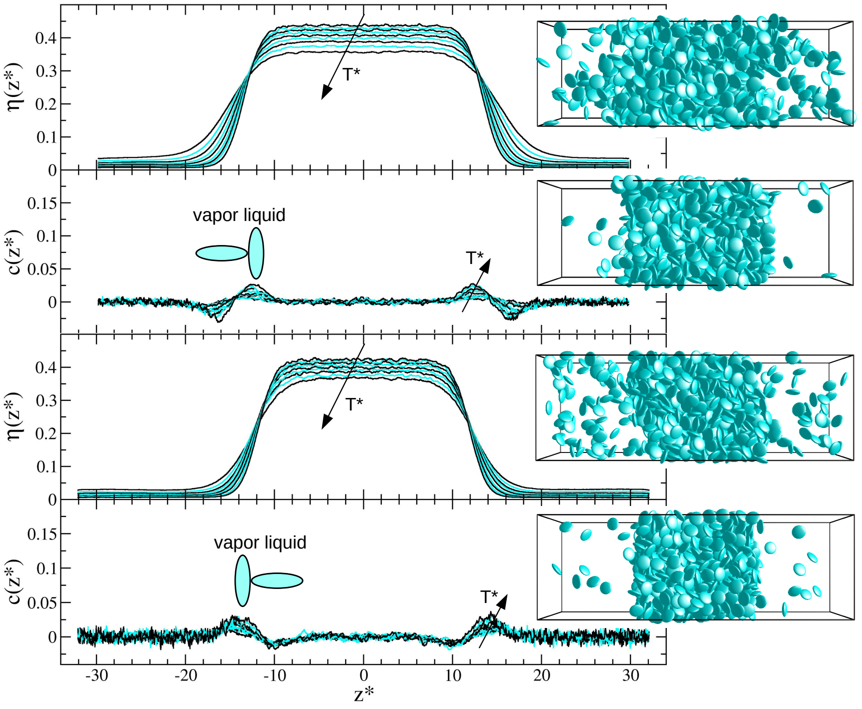

Figure 3. Packing fraction, $\eta(z^*)$, and orientational, $c(z^*)$, profiles along the direction perpendicular to the interfaces for several temperatures close to the critical one. The two upper panels correspond to $\lambda_\perp = 0.5$ and $\lambda_\parallel = 0$ (equator attraction), whereas the two bottom ones to $\lambda_\perp = 0$ and $\lambda_\parallel = 1$ (pole attraction). The snapshots correspond to the highest and the lowest temperatures of both systems. The cartoons exagerate the orientations of the particles at the interface. Note that θ_z is the angle between the z axis and the short axis of the ellipsoid, i.e. $c(z^*)$ is positive for planar and negative for homeotropic anchoring at the interface.

condition [54], one reaches $P_{\rm acc} = \min(1, \exp[(\beta_j - \beta_i)(U_i - U_j)])$, $P_{\rm acc}$ being the swap acceptance probability, $U_i - U_j$ the potential energy difference between replicas i and j, and $\beta_i - \beta_j$ the difference between the reciprocal temperatures i and j ($\beta = 1/(\epsilon T^*)$). Adjacent temperatures should be close enough to provide large exchange acceptance rates between neighboring ensembles.

The largest side of our prismatic boxes triple the others, $L_x = L_y = L_z/3$. We initiate each simulation cell with all $N = 1000$ particles randomly and orientationally placed within its central region, surrounded by vacuum, in such a way that the total packing fraction, $\eta = Nv_0/V$, is around 0.12. Here, $v_0 = \pi\sigma_{\parallel,\rm i}\sigma^2_{\perp,\rm i}/6$ is the volume of the oblate. The system's center of mass is placed and kept during the runs at the cell center. Periodic boundary conditions are employed in the three directions. Verlet lists are implemented to improve performance [55]. Since the goal of these simulations is to study the liquid-vapor coexistence, the highest temperature is set close to and below the critical temperature, and the rest follows a geometrically decreasing trend [56]. Maximum displacements and rotations are varied to yield acceptance rates close to 0.3 during thermalization. Once we observe the complete set of replicas reach a steadystate we start the production runs, which are ended when the packing density profiles, $\eta(z^* = z/\sigma_{\parallel,\mathrm{i}})$, look reasonably noiseless. We compute the liquid, η_l, and vapor, η_v, densities from the center and borders of the cell, respectively (see Fig. 3).

5. Results

Fig. 3 shows $\eta(z^*)$ for equator and pole attraction with $\kappa = 1/3$ (recall that this parameter is fixed in this study). The ten curves correspond to the different temperatures, T^*. With increasing temperature, the difference between vapor and liquid densities diminishes, as is the common behavior for all liquid-vapor coexistences. In addition, the width of the interface widens implying a decrease in surface tension. By approaching the critical point, η_v and η_l converge to η_c, the critical packing fraction, at T_c^*, the critical temperature. At this point, interfaces disappear and the two phases turn into a single one. Note that it is important to observe well-established plateaus for both liquid and vapor phases to yield a good measure of η_l and η_v. We discard data that do not achieve this condition. The snapshots inserted in Fig. 3 correspond to the highest (placed at the top) and the lowest (placed at the bottom) temperatures, where we can observe the liquid-vapor coexistence. Also, the orientation profiles, $c(z^*) = \langle P_2(\cos(\theta_z))\rangle$, show no sign of anisotropy as they fluctuate around zero. In this last expression, $\langle ...\rangle$ stands for ensemble and configuration average, $P_2(x)$ is the second Legendre polynomial, and θ_z is the angle between the z-direction of the simulation cell and the particle's axis of revolution placed at z^*. Only at the interfaces $c(z^*)$ takes values slightly different from zero, positively and negatively peaking at their sides for the equator attraction. Conversely, the opposite occurs for pole attraction. In the first case, the positive peaks appear at the liquid side, signaling a tendency for the particles to align their axes of revolution perpendicular to the interfaces, and the negative ones at the vapor side. This way the particles at the interface decrease their potential energy, irrespective of having equator or uniform (not shown) attraction. This contrast with the pole case, where there is a slight tendency to arrange particles at the liquid interface with their axes perpendicular to the interfaces as found for the Stockmayer fluid [57] (compare the $c(z^*)$ panels of Fig. 3). In all cases, the structure of the interface grows with decreasing temperature.

The critical temperature, T_c^*, is calculated by using the rectilinear diameters law, and the critical packing fraction, η_c, is obtained from a power law temperature dependence of the packing fraction difference of the liquid and vapor phases. For this dependence, we assume a universal value of 0.325 [54, 58] for the critical exponent. Both are extrapolations from the liquid and vapor branches towards the critical point, and so they constitute indirect determinations. Thus, T_c^* and η_c depend on the quality of the η_l and η_v data and the proximity of these data to the critical point. In all cases, we estimate them to have an error of less than 5%.

The right panel of Fig. 4 shows $T_r = T^*/T_c^*$ against $\eta_r = \eta/\eta_c$ for the uniform cases having different $\lambda_\parallel = \lambda_\perp$ values (data are given in the Appendix A). One can

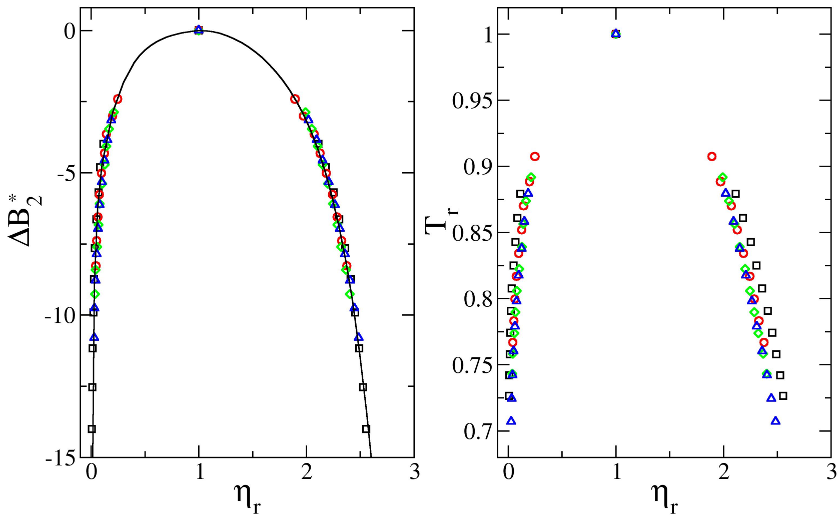

Figure 4. Liquid-vapor phase diagrams for uniform attraction, $\lambda_{\parallel} = \lambda_{\perp} = \lambda$. The left panel shows the ΔB_2^*-η_r construction, whereas the right one depicts the van der Waals representation. Black squares, red circles, green diamonds, and blue triangles correspond to $\lambda = 0.25$, 0.5, 0.75, and 1.0, respectively. The solid line is a guide to the eye.

observe that decreasing the attraction range yields only a slight opening of the liquid and vapor branches. Hence, one may say that the corresponding states law is approximately fulfilled. However, being strict, one may also say that changing λ yields different $T_r(\eta_r)$ curves, which constitutes a violation of the corresponding states law.

The left-hand panel of Fig. 4 shows the same data but replacing T_r with the so-called reduced and shifted second virial coefficient, $\Delta B_2^*(T^*)$ (the corresponding data are given in Appendix A). For this purpose, one need to evaluate $\langle V_{\rm exc}^{\rm HE} \rangle$ and $\langle V_{\rm exc}^{\rm SW} \rangle$. We have estimated it by fixing the position and orientation of a central particle and computing the distance of the closest approach for several positions and orientations of a second one (for higher virial coefficients of hard-ellipsoids see [27]). In the Appendix D, we include a table with these data obtained from a million random configurations. The left panel of Fig. 4 shows an improvement of the data collapse found in its corresponding right panel. Indeed, we do not see a consistent shift of the branches with λ, confirming the theoretical results even for short-range attraction, and implying that the details of the local structure do not affect the $\Delta B_2^*(\eta_r)$ curves. As shown further in the text, the local structure for uniform, equator, and pole attraction are indeed different, despite having a similar ΔB_2^* and η_r value.

The theoretical predictions and the fact of obtaining a good data collapse for uniform attraction encouraged us to explore the extended principle for the equator and pole cases. Nonetheless, it could have been another choice. Indeed, imposing attraction by the edges (equator) and repulsion by the sides (pole) should lead to a simple clay model, which, to our understanding, has not been studied. If equator and

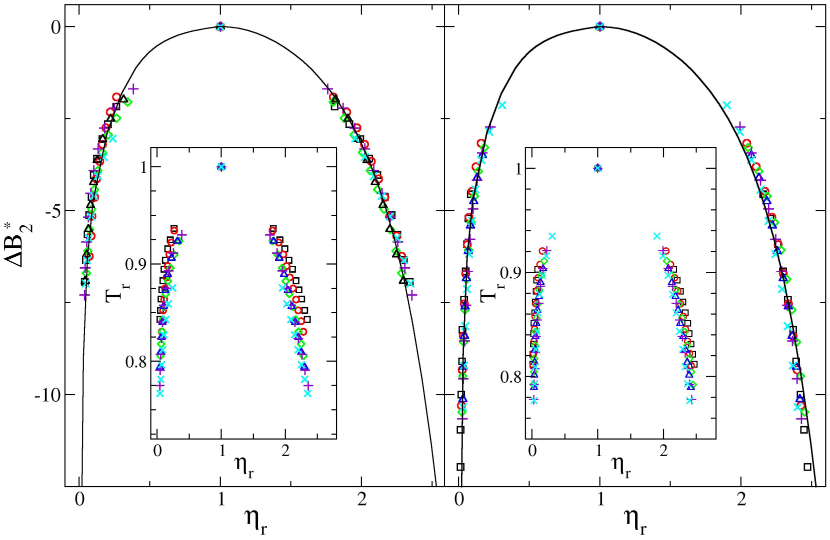

Figure 5. Liquid-vapor phase diagrams for equator attraction (left), $\lambda_{\|} = 0$ and $\lambda = \lambda_{\perp}$, and pole attraction (right), $\lambda_{\perp} = 0$ and $\lambda = \lambda_{\|}$. The mainframes show the ΔB_2^*-η_r construction and the insets the van der Waals representation. Black squares, red circles, green diamonds, blue triangles, violet plus symbols, and cyan crosses correspond to $\lambda = 0.25$, 0.5, 0.75, 1.0, 1.25, and 1.5, respectively. The solid lines are the same guides to the eye than shown in Fig. 4.

pole attractions prove to follow the extended corresponding states law, then we may expect other square-well attractive shapes to yield similar results. Fig. 5 shows the equator (left panel) and pole (right panel) cases. The insets provide the classical $T_r(\eta_r)$ charts for comparison (these data are given in the Appendixes B and C). Also, the panels include the same solid-line inserted in the left panel of Fig. 4 as a guide to the eye. As it can be seen, equator and pole attractions lead to a good data collapse, producing a master curve. Moreover, uniform, equator, and pole attractions at least partially lie above the same reference line. However, the agreement with this line is better for the equator case. In fact, the liquid branch for the pole case is above this curve close to the critical point and crosses to yield data below this curve when moving away from it. Note that the corresponding $T_r(\eta_r)$ inserts of Fig. 5 point out the failure of the data to define a master curve.

Although a bit redundant, it is nice to see all data plotted together. Fig. 6 shows the liquid-vapor curves as obtained from uniform (black symbols), equator (red symbols), and pole attraction (green simbols). This figure makes clear the practical independence of the data from the shape and attractive-range of the attractive shell, confirming the theoretical predictions. As expected, the data collapse is good, contrasting with the same data shown in the corresponding inset. In this last case, both the shape of the attractive shell and the attraction-range hinders the definition of a master curve.

The fulfilment of a corresponding states law makes us wonder about how similar

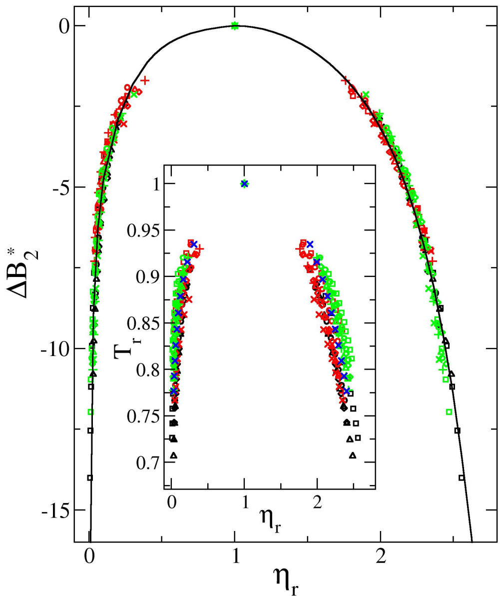

Figure 6. Liquid-vapor phase diagrams for uniform (black symbols), equator (red symbols), and pole (green symbols) attraction. The mainframe shows the ΔB_2^*-η_r construction and the inset the van der Waals representation. Squares, circles, diamonds, triangles, plus symbols, and crosses correspond to λ = 0.25, 0.5, 0.75, 1.0, 1.25, and 1.5, respectively. The solid line is the same guide to the eye than shown in Figs. 4 and 5.

is the local structure of the different liquids sharing the same ΔB_2^* (and η_r) but having different shell shapes. Fig. 7 shows the radial distribution function, $g(r^* = r/\sigma_{\|,\mathrm{i}})$, and orientational distribution function, $c(r^*) =< P_2(\cos(\theta_{r^*})) >$, for uniform, equator, and pole cases with $\lambda = 0.75$, and $\Delta B_2^* = -0.8$. That is, the liquid phases are in a corresponding state. To build this figure we have performed NVT MC simulations of a single liquid phase in a cubic cell, by setting T^* and η consistent with $\Delta B_2^* = -0.8$. The insets of Fig. 7 display the corresponding snapshots. It can be seen that the liquid structures, although similar, are not the same. They share that parallel configurations are not very frequent, since there is not a peak in the $g(r^*)$ close to $r^* = 1$, and the main peaks are always close to $r^* = 2.0$, the location of a perfect T-shape configuration. Thus, T-shapes dominate over parallel configurations, in all cases, even for the pole attraction. Keep in mind that $c(r^*) > 0$ ($c(r^*) < 0$) points to a dominance of parallel (T-shape) configurations, and $c(r^*) = 0$ means an isotropic distribution. For all cases, $c(r^*) = 0$ at relatively large r^*, consistent with an isotropic phase.

Structural differences among the cases are subtle, but they are present. The main peak is wider and lower for uniform and equator attraction than for pole attraction. In addition, the equator first peak shows a peculiar shape, suggesting the contributions of a couple of different configurations. Furthermore, the $c(r^*)$ depression (negative values) pointing out the dominance of the T-shape configuration associated with the

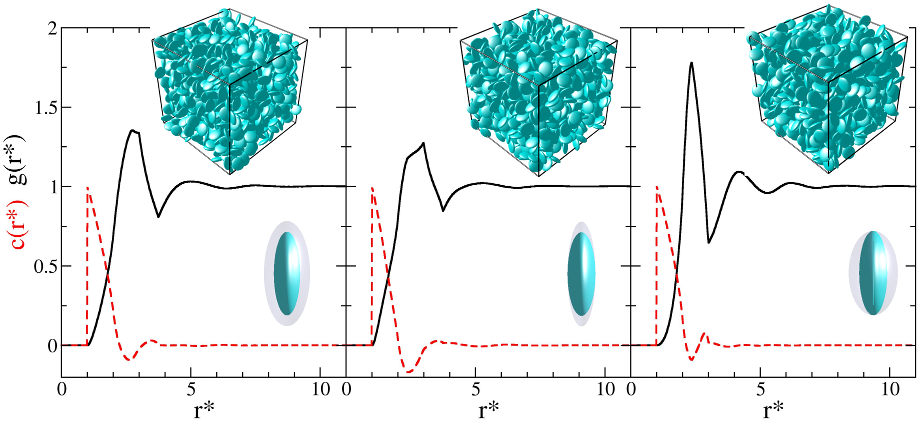

Figure 7. Radial distribution functions, $g(r^*)$, and orientational distribution functions, $c(r^*)$, for liquid phases. The left, middle, and right panels correspond to uniform, equator, and pole attraction, respectively, having $\lambda = 0.75$ and the same corresponding state, $\Delta B_2^* = -0.8$. Density (temperature) increases (decreases) from left to right. The insets show the corresponding snapshots. Different models are depicted by the inserted drawings.

principal peaks is more pronounced in this case. This fact, together with the knowledge of the potential shape, suggests a more fragile T-shape arrangement since slight particles rotations away from the perpendicular angle would produce a binding breakage. In contrast, T-shapes for the pole case are more frequent, as indicated by the height of the main peak, but more flexible, as suggested by the not-so-deep $c(r^*)$.

6. Conclusion

We have shown through theoretical arguments that the liquid-vapor coexistence in the ΔB_2^*-η_r plane is independent of the details of the attractive part of the pair-potential for any shape of a given hardcore. The only imposed restriction is that attraction is taken into account as a perturbation at the second virial level. As a result, the theoretical calculations for the long-range square-well potential yield the same master curve as simulations. Nonetheless, this restriction makes its results questionable for short-range attraction, where the local structure is expected to play a major role.

To explore whether a master curve is still achieved for an anisotropic hardcore shape and different shapes of the attraction shell, we have performed REMC simulations at the short-range regime. We have fixed the hardcore shape to be an oblate of $\kappa = 1/3$ and considered three different types of attraction: uniform, equator, and pole. These attraction types are produced by accounting for attractive ellipsoidal shells sharing the same center and axis of revolution as the hardcore. For all studied cases, and in line with the theoretical outcomes, we have found a single master curve for the liquid-vapor coexistence in the ΔB_2^*-η_r plane.

Given this finding, we have explored liquids sharing the same ΔB_2^* and η_r values but different shell shapes. We have confirmed that there are differences among the local structures of the fluids. Hence, one should conclude that despite these differences, the extended law of corresponding states holds as a good approximation even for asymmetric cores and potential ranges of different shape and attractive range.

We think the extended corresponding principle may also apply to other anisotropic attractive colloids [59, 60, 61, 47, 48] when varying the shell shape and the attractive ranges, or even when varying the core shape. However, the law may break down for extremely short-range potentials, where the liquid-vapor coexistence turns metastable [62].

7. Acknowledgements

The authors thank financial support through project A1-S-9197 from CONACyT. MGdeS also acknowledges CONACyT for a scholarship. VS and GP acknowledge the National Research, Development, and Innovation Office - K 137720 for financial support.

8. Data availability statement

All data that support the findings of this study are included within the appendixes of this article.

9. Appendix A: liquid-vapor coexistence for uniform attraction

Table 1. Liquid-vapor coexistence data for the uniform attraction case with $\lambda_\parallel = \lambda_\perp = 0.25$. Note that the first line corresponds to the estimated critical point. Volume units of B_2 are given in terms of the shortest axis of the hardcore, $\sigma^3_{\parallel,\mathrm{i}}$.

T^*	T_r	η_v	η_l	$\eta_{\mathrm{v}r}$	$\eta_{\mathrm{l}r}$	B_2	ΔB_2^*
0.523	1.0000	0.192	0.192	1.0000	1.0000	-27.981	0.0000
0.4600	0.8793	0.0219	0.4056	0.1142	2.1127	-46.758	-3.9847
0.4503	0.8608	0.0163	0.4186	0.0851	2.1803	-50.642	-4.8088
0.4409	0.8427	0.0131	0.4326	0.0684	2.2533	-54.802	-5.6915
0.4316	0.8250	0.0095	0.4427	0.0495	2.3058	-59.260	-6.6375
0.4226	0.8077	0.0065	0.4532	0.0340	2.3603	-64.045	-7.6531
0.4137	0.7908	0.0050	0.4631	0.0260	2.4122	-69.180	-8.7427
0.4050	0.7741	0.0040	0.4711	0.0208	2.4534	-74.705	-9.9152
0.3965	0.7579	0.0027	0.4783	0.0143	2.4911	-80.654	-11.178
0.3882	0.7420	0.0021	0.4853	0.0109	2.5275	-87.065	-12.538
0.3800	0.7264	0.0014	0.4908	0.0071	2.5561	-93.977	-14.005

Table 2. Liquid-vapor coexistence data for the uniform attraction case with $\lambda_\parallel = \lambda_\perp = 0.5$. Note that the first line corresponds to the estimated critical point. Volume units of B_2 are given in terms of the shortest axis of the hardcore, $\sigma^3_{\parallel,\mathrm{i}}$.

T^*	T_r	η_v	η_l	$\eta_{\mathrm{v}r}$	$\eta_{\mathrm{l}r}$	B_2	ΔB_2^*
0.750	1.0000	0.165	0.165	1.0000	1.0000	-32.061	0.0000
0.6805	0.9074	0.0410	0.3126	0.2485	1.8945	-43.429	-2.4125
0.6663	0.8884	0.0330	0.3256	0.2000	1.9732	-46.269	-3.0150
0.6525	0.8699	0.0236	0.3423	0.1432	2.0744	-49.259	-3.6495
0.6389	0.8518	0.0209	0.3514	0.1267	2.1295	-52.416	-4.3192
0.6255	0.8341	0.0163	0.3609	0.0988	2.1870	-55.744	-5.0257
0.6125	0.8167	0.0129	0.3703	0.0781	2.2443	-59.263	-5.7724
0.5997	0.7997	0.0108	0.3775	0.0652	2.2876	-62.980	-6.5612
0.5872	0.7830	0.0088	0.3844	0.0535	2.3295	-66.913	-7.3959
0.5750	0.7667	0.0073	0.3923	0.0444	2.3775	-71.078	-8.2796

Table 3. Liquid-vapor coexistence data for the uniform attraction case with $\lambda_{\parallel} = \lambda_{\perp} = 0.75$. Note that the first line corresponds to the estimated critical point. Volume units of B_2 are given in terms of the shortest axis of the hardcore, $\sigma^3_{\parallel,\mathrm{i}}$.

T^*	T_r	η_{v}	η_{l}	$\eta_{\mathrm{v}r}$	$\eta_{\mathrm{l}r}$	B_2	ΔB_2^*
0.942	1.0000	0.147	0.147	1.0000	1.0000	-39.089	0.0000
0.8400	0.8917	0.0313	0.2930	0.2126	1.9931	-52.643	-2.8761
0.8232	0.8738	0.0244	0.3014	0.1660	2.0501	-55.407	-3.4628
0.8067	0.8563	0.0207	0.3093	0.1409	2.1044	-58.297	-4.0759
0.7905	0.8391	0.0187	0.3161	0.1269	2.1504	-61.322	-4.7179
0.7746	0.8223	0.0152	0.3235	0.1036	2.2006	-64.488	-5.3898
0.7591	0.8058	0.0117	0.3304	0.0797	2.2477	-67.807	-6.0940
0.7439	0.7897	0.0100	0.3363	0.0684	2.2875	-71.283	-6.8316
0.7289	0.7738	0.0084	0.3417	0.0575	2.3243	-74.929	-7.6054
0.7143	0.7583	0.0063	0.3482	0.0430	2.3687	-78.752	-8.4167
0.7000	0.7431	0.0054	0.3532	0.0368	2.4024	-82.769	-9.2692

Table 4. Liquid-vapor coexistence data for the uniform attraction case with $\lambda_\parallel = \lambda_\perp = 1.0$. Note that the first line corresponds to the estimated critical point. Volume units of B_2 are given in terms of the shortest axis of the hardcore, $\sigma^3_{\parallel,\mathrm{i}}$.

T^*	T_r	η_v	η_l	$\eta_{\mathrm{v}r}$	$\eta_{\mathrm{l}r}$	B_2	ΔB_2^*
1.160	1.0000	0.135	0.135	1.0000	1.0000	-43.098	0.0000
1.0200	0.8793	0.0251	0.2728	0.1861	2.0207	-57.979	-3.1579
0.9956	0.8582	0.0205	0.2827	0.1518	2.0939	-61.227	-3.8472
0.9717	0.8377	0.0169	0.2903	0.1250	2.1506	-64.637	-4.5708
0.9484	0.8176	0.0133	0.2981	0.0986	2.2081	-68.219	-5.3309
0.9257	0.7980	0.0106	0.3057	0.0789	2.2646	-71.983	-6.1297
0.9035	0.7789	0.0086	0.3118	0.0639	2.3100	-75.943	-6.9700
0.8819	0.7602	0.0069	0.3185	0.0511	2.3589	-80.111	-7.8545
0.8608	0.7420	0.0056	0.3247	0.0413	2.4051	-84.500	-8.7859
0.8401	0.7243	0.0044	0.3302	0.0328	2.4456	-89.125	-9.7672
0.8200	0.7069	0.0038	0.3355	0.0282	2.4856	-94.002	-10.802

10. Appendix B: liquid-vapor coexistence for equator attraction

Table 5. Liquid-vapor coexistence data for the equator attraction case with $\lambda_{\|} = 0$ and $\lambda_{\perp} = 0.25$. Note that the first line corresponds to the estimated critical point. Volume units of B_2 are given in terms of the shortest axis of the hardcore, $\sigma^3_{\|,\mathrm{i}}$.

T^*	T_r	η_{v}	η_{l}	$\eta_{\mathrm{v}r}$	$\eta_{\mathrm{l}r}$	B_2	ΔB_2^*
0.427	1.0000	0.192	0.192	1.0000	1.0000	-28.692	0.0000
0.4000	0.9368	0.0504	0.3474	0.2623	1.8095	-38.931	-2.1728
0.3950	0.9251	0.0390	0.3674	0.2029	1.9136	-41.182	-2.6505
0.3910	0.9157	0.0314	0.3821	0.1636	1.9899	-43.079	-3.0530
0.3860	0.9040	0.0242	0.3945	0.1258	2.0547	-45.577	-3.5831
0.3820	0.8946	0.0198	0.4054	0.1029	2.1116	-47.686	-4.0305
0.3770	0.8829	0.0166	0.4157	0.0867	2.1651	-50.469	-4.6211
0.3730	0.8735	0.0136	0.4249	0.0707	2.2130	-52.822	-5.1205
0.3690	0.8642	0.0113	0.4329	0.0588	2.2545	-55.297	-5.6457
0.3640	0.8525	0.0091	0.4415	0.0474	2.2996	-58.573	-6.3410
0.3600	0.8431	0.0077	0.4495	0.0403	2.3411	-61.353	-6.9308

Table 6. Liquid-vapor coexistence data for the equator attraction case with $\lambda_{\|} = 0$ and $\lambda_{\perp} = 0.5$. Note that the first line corresponds to the estimated critical point. Volume units of B_2 are given in terms of the shortest axis of the hardcore, $\sigma^3_{\|,\mathrm{i}}$.

T^*	T_r	η_{v}	η_{l}	$\eta_{\mathrm{v}r}$	$\eta_{\mathrm{l}r}$	B_2	ΔB_2^*
0.578	1.0000	0.179	0.179	1.0000	1.0000	-31.776	1.0000
0.5400	0.9343	0.0472	0.3221	0.2637	1.7997	-40.765	-1.9075
0.5329	0.9220	0.0396	0.3391	0.2211	1.8943	-42.718	-2.3220
0.5260	0.9099	0.0339	0.3520	0.1894	1.9666	-44.742	-2.7514
0.5191	0.8981	0.0295	0.3617	0.1651	2.0208	-46.841	-3.1970
0.5123	0.8863	0.0261	0.3703	0.1457	2.0686	-49.017	-3.6586
0.5057	0.8748	0.0220	0.3795	0.1227	2.1199	-51.274	-4.1376
0.4991	0.8635	0.0195	0.3876	0.1091	2.1656	-53.616	-4.6345
0.4926	0.8523	0.0162	0.3938	0.0903	2.1998	-56.049	-5.1510
0.4863	0.8413	0.0152	0.4026	0.0847	2.2491	-58.571	-5.6860
0.4800	0.8304	0.0127	0.4086	0.0711	2.2829	-61.190	-6.2419

Table 7. Liquid-vapor coexistence data for the equator attraction case with $\lambda_{\parallel} = 0$ and $\lambda_{\perp} = 0.75$. Note that the first line corresponds to the estimated critical point. Volume units of B_2 are given in terms of the shortest axis of the hardcore, $\sigma^3_{\parallel,\mathrm{i}}$.

T^*	T_r	η_{v}	η_{l}	$\eta_{\mathrm{v}r}$	$\eta_{\mathrm{l}r}$	B_2	ΔB_2^*
0.720	1.0000	0.166	0.166	1.0000	1.0000	-34.124	0.0000
0.6650	0.9236	0.0570	0.2986	0.3435	1.7987	-43.768	-2.0465
0.6550	0.9097	0.0440	0.3116	0.2651	1.8770	-45.838	-2.4858
0.6451	0.8960	0.0341	0.3231	0.2053	1.9467	-47.989	-2.9422
0.6354	0.8825	0.0273	0.3329	0.1644	2.0055	-50.225	-3.4167
0.6258	0.8691	0.0219	0.3423	0.1316	2.0619	-52.550	-3.9101
0.6163	0.8560	0.0179	0.3508	0.1076	2.1134	-54.969	-4.4234
0.6071	0.8431	0.0149	0.3585	0.0896	2.1594	-57.486	-4.9575
0.5979	0.8304	0.0123	0.3658	0.0743	2.2038	-60.107	-5.5136
0.5889	0.8179	0.0101	0.3727	0.0610	2.2450	-62.835	-6.0927
0.5800	0.8056	0.0084	0.3792	0.0505	2.2842	-65.679	-6.6961

Table 8. Liquid-vapor coexistence data for the equator attraction case with $\lambda_{\parallel} = 0$ and $\lambda_{\perp} = 1$. Note that the first line corresponds to the estimated critical point. Volume units of B_2 are given in terms of the shortest axis of the hardcore, $\sigma^3_{\parallel,\mathrm{i}}$.

T^*	T_r	η_{v}	η_{l}	$\eta_{\mathrm{v}r}$	$\eta_{\mathrm{l}r}$	B_2	ΔB_2^*
0.850	1.0000	0.160	0.160	1.0000	1.0000	-37.778	0.0000
0.7850	0.9236	0.0504	0.2905	0.3150	1.8158	-47.110	-1.9803
0.7704	0.9063	0.0356	0.3045	0.2226	1.9030	-49.582	-2.5049
0.7560	0.8894	0.0265	0.3165	0.1658	1.9778	-52.164	-3.0527
0.7418	0.8727	0.0205	0.3262	0.1279	2.0386	-54.861	-3.6251
0.7279	0.8564	0.0162	0.3354	0.1014	2.0960	-57.681	-4.2234
0.7143	0.8404	0.0128	0.3443	0.0803	2.1518	-60.630	-4.8492
0.7010	0.8247	0.0104	0.3521	0.0652	2.2009	-63.715	-5.5039
0.6879	0.8093	0.0084	0.3597	0.0526	2.2479	-66.945	-6.1894
0.6750	0.7941	0.0068	0.3674	0.0427	2.2961	-70.328	-6.9073

Table 9. Liquid-vapor coexistence data for the equator attraction case with $\lambda_{\parallel} = 0$ and $\lambda_{\perp} = 1.25$. Note that the first line corresponds to the estimated critical point. Volume units of B_2 are given in terms of the shortest axis of the hardcore, $\sigma^3_{\parallel,{\rm i}}$.

T^*	T_r	$\eta_{\rm v}$	$\eta_{\rm l}$	$\eta_{{\rm v}r}$	$\eta_{{\rm l}r}$	B_2	ΔB_2^*
1.000	1.0000	0.153	0.153	1.0000	1.0000	-39.131	0.0000
0.9300	0.9300	0.0586	0.2692	0.3833	1.7592	-47.105	-1.6921
0.9114	0.9114	0.0382	0.2859	0.2494	1.8684	-49.551	-2.2113
0.8931	0.8931	0.0274	0.2986	0.1793	1.9516	-52.105	-2.7531
0.8752	0.8752	0.0205	0.3094	0.1337	2.0221	-54.769	-3.3186
0.8576	0.8576	0.0158	0.3192	0.1032	2.0864	-57.553	-3.9092
0.8404	0.8404	0.0125	0.3284	0.0816	2.1464	-60.461	-4.5264
0.8236	0.8236	0.0100	0.3371	0.0656	2.2031	-63.501	-5.1715
0.8070	0.8070	0.0081	0.3452	0.0528	2.2564	-66.680	-5.8462
0.7909	0.7909	0.0065	0.3529	0.0426	2.3065	-70.007	-6.5522
0.7750	0.7750	0.0058	0.3604	0.0382	2.3558	-73.490	-7.2914

Table 10. Liquid-vapor coexistence data for the equator attraction case with $\lambda_{\parallel} = 0$ and $\lambda_{\perp} = 1.5$. Note that the first line corresponds to the estimated critical point. Volume units of B_2 are given in terms of the shortest axis of the hardcore, $\sigma^3_{\parallel,{\rm i}}$.

T^*	T_r	$\eta_{\rm v}$	$\eta_{\rm l}$	$\eta_{{\rm v}r}$	$\eta_{{\rm l}r}$	B_2	ΔB_2^*
1.180	1.0000	0.148	0.148	1.0000	1.0000	-38.637	0.0000
1.0332	0.8756	0.0352	0.2894	0.2380	1.9553	-52.968	-3.0411
1.0138	0.8591	0.0256	0.2995	0.1732	2.0234	-55.325	-3.5412
0.9948	0.8430	0.0197	0.3084	0.1329	2.0839	-57.771	-4.0604
0.9761	0.8272	0.0154	0.3174	0.1039	2.1448	-60.313	-4.5997
0.9579	0.8117	0.0123	0.3254	0.0829	2.1990	-62.953	-5.1600
0.9399	0.7965	0.0099	0.3330	0.0670	2.2502	-65.698	-5.7424
0.9223	0.7816	0.0082	0.3403	0.0551	2.2991	-68.552	-6.3480
0.9050	0.7669	0.0067	0.3471	0.0452	2.3454	-71.520	-6.9780

11. Appendix C: liquid-vapor coexistence for pole attraction

Table 11. Liquid-vapor coexistence data for the pole attraction case with $\lambda_{\parallel} = 0.25$ and $\lambda_{\perp} = 0$. Note that the first line corresponds to the estimated critical point. Volume units of B_2 are given in terms of the shortest axis of the hardcore, $\sigma^3_{\parallel,\mathrm{i}}$.

T^*	T_r	η_{v}	η_{l}	$\eta_{\mathrm{v}r}$	$\eta_{\mathrm{l}r}$	B_2	ΔB_2^*
0.340	1.0000	0.221	0.221	1.0000	1.0000	-29.267	0.0000
0.3070	0.9029	0.0189	0.4764	0.0854	2.1558	-50.706	-4.5495
0.3034	0.8923	0.0151	0.4880	0.0683	2.2081	-53.832	-5.2129
0.2998	0.8818	0.0130	0.4995	0.0588	2.2600	-57.120	-5.9107
0.2963	0.8715	0.0109	0.5077	0.0494	2.2971	-60.581	-6.6451
0.2928	0.8612	0.0084	0.5153	0.0382	2.3316	-64.227	-7.4187
0.2894	0.8511	0.0059	0.5234	0.0268	2.3683	-68.068	-8.2338
0.2860	0.8411	0.0053	0.5281	0.0242	2.3894	-72.116	-9.0929
0.2826	0.8312	0.0038	0.5350	0.0174	2.4207	-76.385	-9.9988
0.2793	0.8214	0.0028	0.5406	0.0129	2.4460	-80.890	-10.955
0.2760	0.8118	0.0029	0.5459	0.0130	2.4703	-85.647	-11.964

Table 12. Liquid-vapor coexistence data for the pole attraction case with $\lambda_{\parallel} = 0.5$ and $\lambda_{\perp} = 0$. Note that the first line corresponds to the estimated critical point. Volume units of B_2 are given in terms of the shortest axis of the hardcore, $\sigma^3_{\parallel,\mathrm{i}}$.

T^*	T_r	η_{v}	η_{l}	$\eta_{\mathrm{v}r}$	$\eta_{\mathrm{l}r}$	B_2	ΔB_2^*
0.427	1.0000	0.204	0.204	1.0000	1.0000	-34.709	0.0000
0.3930	0.9204	0.0324	0.4161	0.1588	2.0399	-49.631	-3.1667
0.3875	0.9074	0.0249	0.4300	0.1219	2.1079	-52.637	-3.8044
0.3820	0.8947	0.0194	0.4423	0.0953	2.1682	-55.798	-4.4752
0.3767	0.8821	0.0150	0.4527	0.0735	2.2190	-59.125	-5.1812
0.3714	0.8697	0.0123	0.4616	0.0604	2.2627	-62.629	-5.9248
0.3662	0.8575	0.0101	0.4692	0.0495	2.3000	-66.321	-6.7083
0.3610	0.8454	0.0082	0.4763	0.0404	2.3348	-70.214	-7.5343
0.3559	0.8336	0.0067	0.4832	0.0329	2.3687	-74.319	-8.4055
0.3509	0.8219	0.0050	0.4890	0.0243	2.3971	-78.651	-9.3249
0.3460	0.8103	0.0038	0.4944	0.0188	2.4234	-83.227	-10.296

Table 13. Liquid-vapor coexistence data for the pole attraction case with $\lambda_{\|} = 0.75$ and $\lambda_{\perp} = 0$. Note that the first line corresponds to the estimated critical point. Volume units of B_2 are given in terms of the shortest axis of the hardcore, $\sigma^3_{\|,\mathrm{i}}$.

T^*	T_r	η_{v}	η_{l}	$\eta_{\mathrm{v}r}$	$\eta_{\mathrm{l}r}$	B_2	ΔB_2^*
0.505	1.0000	0.187	0.187	1.0000	1.0000	-37.058	0.0000
0.4600	0.9109	0.0342	0.3834	0.1827	2.0505	-52.535	-3.2839
0.4529	0.8969	0.0259	0.3977	0.1387	2.1268	-55.575	-3.9293
0.4459	0.8830	0.0210	0.4087	0.1121	2.1856	-58.771	-4.6076
0.4391	0.8694	0.0163	0.4185	0.0872	2.2379	-62.133	-5.3210
0.4323	0.8560	0.0130	0.4269	0.0694	2.2827	-65.670	-6.0715
0.4256	0.8428	0.0103	0.4346	0.0553	2.3239	-69.394	-6.8618
0.4191	0.8299	0.0084	0.4412	0.0447	2.3596	-73.316	-7.6941
0.4126	0.8171	0.0066	0.4475	0.0355	2.3932	-77.451	-8.5715
0.4063	0.8045	0.0054	0.4529	0.0289	2.4220	-81.811	-9.4968
0.4000	0.7921	0.0043	0.4582	0.0230	2.4504	-86.412	-10.473

Table 14. Liquid-vapor coexistence data for the pole attraction case with $\lambda_{\|} = 1$ and $\lambda_{\perp} = 0$. Note that the first line corresponds to the estimated critical point. Volume units of B_2 are given in terms of the shortest axis of the hardcore, $\sigma^3_{\|,\mathrm{i}}$.

T^*	T_r	η_{v}	η_{l}	$\eta_{\mathrm{v}r}$	$\eta_{\mathrm{l}r}$	B_2	ΔB_2^*
0.570	1.0000	0.177	0.177	1.0000	1.0000	-40.779	0.0000
0.5150	0.9035	0.0298	0.3668	0.1683	2.0726	-57.256	-3.4965
0.5073	0.8901	0.0231	0.3764	0.1304	2.1267	-60.125	-4.1053
0.4998	0.8768	0.0188	0.3863	0.1059	2.1823	-63.126	-4.7422
0.4924	0.8638	0.0146	0.3932	0.0824	2.2217	-66.267	-5.4086
0.4850	0.8509	0.0119	0.3993	0.0671	2.2561	-69.549	-6.1051
0.4778	0.8383	0.0097	0.4069	0.0547	2.2987	-72.990	-6.8353
0.4707	0.8258	0.0079	0.4131	0.0446	2.3338	-76.592	-7.5998
0.4637	0.8135	0.0071	0.4180	0.0403	2.3616	-80.365	-8.4005
0.4568	0.8014	0.0059	0.4232	0.0334	2.3911	-84.324	-9.2405
0.4500	0.7895	0.0052	0.4277	0.0296	2.4163	-88.478	-10.122

Table 15. Liquid-vapor coexistence data for the pole attraction case with $\lambda_{\|} = 1.25$ and $\lambda_{\perp} = 0$. Note that the first line corresponds to the estimated critical point. Volume units of B_2 are given in terms of the shortest axis of the hardcore, $\sigma^3_{\|,\mathrm{i}}$.

T^*	T_r	η_{v}	η_{l}	$\eta_{\mathrm{v}r}$	$\eta_{\mathrm{l}r}$	B_2	ΔB_2^*
0.630	1.0000	0.167	0.167	1.0000	1.0000	-44.242	0.0000
0.5800	0.9206	0.0374	0.3328	0.2241	1.9927	-57.069	-2.7220
0.5692	0.9035	0.0277	0.3462	0.1661	2.0731	-60.394	-3.4276
0.5587	0.8868	0.0217	0.3572	0.1297	2.1387	-63.895	-4.1704
0.5483	0.8703	0.0170	0.3665	0.1016	2.1945	-67.583	-4.9532
0.5381	0.8542	0.0133	0.3748	0.0794	2.2443	-71.472	-5.7784
0.5281	0.8383	0.0106	0.3821	0.0633	2.2880	-75.576	-6.6492
0.5183	0.8227	0.0085	0.3887	0.0507	2.3278	-79.907	-7.5684
0.5087	0.8075	0.0068	0.3948	0.0406	2.3644	-84.483	-8.5394
0.4993	0.7925	0.0054	0.4003	0.0324	2.3973	-89.321	-9.5659
0.4900	0.7778	0.0044	0.4054	0.0262	2.4276	-94.438	-10.652

Table 16. Liquid-vapor coexistence data for the pole attraction case with $\lambda_{\|} = 1.5$ and $\lambda_{\perp} = 0$. Note that the first line corresponds to the estimated critical point. Volume units of B_2 are given in terms of the shortest axis of the hardcore, $\sigma^3_{\|,\mathrm{i}}$.

T^*	T_r	η_{v}	η_{l}	$\eta_{\mathrm{v}r}$	$\eta_{\mathrm{l}r}$	B_2	ΔB_2^*
0.690	1.0000	0.160	0.160	1.0000	1.0000	-46.838	0.0000
0.6450	0.9348	0.0492	0.3039	0.3075	1.8995	-56.874	-2.1298
0.6319	0.9158	0.0347	0.3186	0.2168	1.9913	-60.291	-2.8549
0.6190	0.8971	0.0256	0.3315	0.1603	2.0719	-63.895	-3.6197
0.6064	0.8788	0.0190	0.3422	0.1190	2.1386	-67.698	-4.4266
0.5941	0.8610	0.0149	0.3510	0.0934	2.1936	-71.713	-5.2788
0.5820	0.8434	0.0118	0.3591	0.0739	2.2446	-75.957	-6.1793
0.5701	0.8263	0.0094	0.3665	0.0587	2.2904	-80.445	-7.1317
0.5585	0.8094	0.0075	0.3728	0.0471	2.3298	-85.194	-8.1396
0.5471	0.7930	0.0060	0.3787	0.0377	2.3666	-90.224	-9.2069
0.5360	0.7768	0.0048	0.3842	0.0298	2.4010	-95.555	-10.338

12. Appendix D: excluded volumes

Table 17. Average volume of the attractive region (including the hardcore) for the square-well model given by Eqs. 10 to 14. Volume units are given in terms of the shortest axis of the hardcore, $\sigma^3_{\|,\mathrm{i}}$. The first line corresponds to the hardcore with $\kappa = 1/3$, $\langle V^{\mathrm{HC}}_{\mathrm{exc}} \rangle$.

	uniform			equator			pole		
λ	$\sigma_\|$	$\sigma_\perp$	$\langle V^{\mathrm{SW}}_{\mathrm{exc}} \rangle$	$\sigma_\|$	$\sigma_\perp$	$\langle V^{\mathrm{SW}}_{\mathrm{exc}} \rangle$	$\sigma_\|$	$\sigma_\perp$	$\langle V^{\mathrm{SW}}_{\mathrm{exc}} \rangle$
0.00	1.00	3.00	50.692	1.00	3.00	50.692	1.00	3.00	50.692
0.25	1.25	3.25	69.198	1.00	3.25	62.188	1.25	3.00	56.781
0.50	1.50	3.50	91.790	1.00	3.50	75.307	1.50	3.00	63.468
0.75	1.75	3.75	118.84	1.00	3.75	90.202	1.75	3.00	70.680
1.00	2.00	4.00	150.75	1.00	4.00	106.98	2.00	3.00	78.360
1.25	2.25	4.25	–	1.00	4.25	125.74	2.25	3.00	86.465
1.50	2.50	4.50	–	1.00	4.50	146.64	2.50	3.00	94.976

References

[1] Guggenheim E A 1945 *J. Chem. Phys.* **13** 253

[2] Hunter R J 1994 *Introduction to Modern Colloid Science* (Oxford: Oxford University Press)

[3] Noro M G and Frenkel D 2000 *J. Chem. Phys.* **113** 2941

[4] Foffi G and Sciortino F 2007 *J. Chem. Phys.* **111** 9702–9705

[5] Platten F, Valadez-Pérez N E, Castañeda Priego R and Egelhaaf S U 2015 *J. Chem. Phys.* **142** 174905

[6] Bucciarelli S, Mahmoudi N, Casal-Dujat L, Jéhannin M, Jud C and Stradner A 2016 *J. Phys. Chem. Lett.* **7** 1610–1615

[7] Valadez-Pérez N E, Liu Y and Castañeda Priego R 2018 *Phys. Rev. Lett.* **120** 248004

[8] van Gruijthuijsen K, Obiols-Rabasa M, Schurtenberger P, Bouwman W G and Stradner A 2018 *Soft Matter* **14** 3704–3715

[9] Salazar J L and Reyes Y 2019 *J. Mol. Liq.* **294** 111606

[10] Benavides A L and Del Río F 2002 *Mol. Phys.* **68** 983–1000

[11] Benavides A L, Alejandre J and Del Río F 1991 *Mol. Phys.* **74** 321–331

[12] Gil-Villegas A, del Río F and Benavides A L 1996 *Fluid Ph. Equilibria* **119** 97

[13] Varga S, Williamson D C and Szalai I 1999 *Mol. Phys.* **96** 1695–1703

[14] Del Río F, Avalos E, Espíndola R, Rull R L F, Jackson G and Lago S 2002 *Mol. Phys.* **109** 2531–2546

[15] Schöll-Paschinger E, Benavides A L and Castañeda Priego R 2005 *J. Chem. Phys.* **123** 234513

[16] Largo J, Miller M A and Sciortino F 2008 *J. Chem. Phys.* **128** 134513

[17] Fu D, Li Y and Wu J 2003 *Phys. Rev. E* **68** 011403

[18] López-Rendón R, Reyes Y and Orea P 2006 *J. Chem. Phys.* **125** 084508

[19] Zhou S 2007 *Mol. Simul.* **33** 1187

[20] Gazzillo D and Pini D 2013 *J. Chem. Phys.* **139** 164501

[21] Orea P, Varga S and Odriozola G 2015 *Chem. Phys. Lett.* **631–632** 26–29

[22] Orea P, Romero-Martínez A, Basurto E, Vargas C A and Odriozola G 2015 *J. Chem. Phys.* **143** 024504

[23] Singh A K, Dey T K and Sinha S K 1990 *Pramana* **34** 123–131

[24] Varga S, Meneses-Juárez E and Odriozola G 2013 *Soft Matter* **9** 11178

[25] Varga S, Meneses-Juárez E and Odriozola G 2014 *J. Chem. Phys.* **140** 134905

[26] Meneses-Juárez E, Varga S, Orea P and Odriozola G 2013 *Soft Matter* **9** 5277

[27] Marienhagen P, Hellmann R and Wagner J 2021 *Phys. Rev. E* **104** 015308

[28] Samborski A and Evans G T 1993 *Molecular Physics* **80** 1257–1261

[29] Orea P, Duda Y, Weiss V C, Schröer W and Alejandre J 2004 *J. Chem. Phys.* **120** 11754

[30] Patel B H, Docherty H, Varga S, Galindo A and Maitland G C 2005 *Mol. Phys.* **103** 129

[31] Pagan D L and Gunton J D 2005 *J. Chem. Phys.* **122** 184515

[32] Liu H, Garde S and Kumar S 2005 *J. Chem. Phys.* **123** 174505

[33] Wegner F J 1972 *Phys. Rev. B* **5**(11) 4529–4536

[34] Vega L, De Miguel E, Rull L F, Jackson G and McLure I A 1992 *J. Chem. Phys.* **96** 2296–2305

[35] García E, Williamson D C and Martínez-Richa A 2000 *Mol. Phys.* **98** 179

[36] Berne B J and Pechukas P 1972 *J. Chem. Phys.* **56** 4195–4205

[37] Rickayzen G 1998 *Mol. Phys.* **95** 393–400

[38] Guevara-Rodríguez F J and Odriozola G 2011 *J. Chem. Phys.* **135**

[39] Bianchi E, Largo J, Tartaglia P, Zaccarelli E and Sciortino F 2006 *Phys. Rev. Lett.* **97** 168301

[40] Almarza N G, Tavares J M, Simões M and Telo Da Gama M M 2011 *J. Chem. Phys.* **135** 174903

[41] Oleksy A and Teixeira P I C 2015 *Phys. Rev. E* **91** 012301

[42] Teixeira P I C 2017 *Colloids Surf. A Physicochem. Eng. Asp.* **514** 56–62

[43] Sciortino F and Zaccarelli E 2017 *Curr. Opin. Colloid Interface Sci.* **30** 90–96

[44] Teixeira P I C and Sciortino F 2019 *J. Chem. Phys.* **113** 174903

[45] Ruzicka B and Zaccarelli E 2011 *Soft Matter* **7** 1268–1286

[46] Ruzicka B, Zaccarelli E, Zulian L, Angelini R, Sztucki M, Moussaïd A, Narayanan T and Sciortino F 2011 *Nature Mater.* **10** 56–60

[47] Pujala R K and Bohidar H B 2015 *Colloid Polym. Sci.* **293** 2883–2890

[48] Pujala R K and Bohidar H B 2019 *Colloid Polym. Sci.* **297** 1053–1065

[49] Boire A, Menut P, Morel M H and Sanchez C 2013 *Soft Matter* **9** 11417

[50] Lyubartsev A P, Martinovski A A, Shevkunov S V and Vorontsov-Velyaminov P N 1992 *J. Chem. Phys.* **96** 1776–1783

[51] Marinari E and Parisi G 1992 *Europhys. Lett.* **19** 451–458

[52] Hukushima K and Nemoto K 1996 *J. Phys. Soc. Jpn.* **65** 1604–1608

[53] Chapela G A, Saville G, Thompson S M and Rowlinson J S 1977 *J. Chem. Soc. Farad. T2* **73** 1133–1144

[54] Frenkel D and Smit B 1996 *Understanding molecular simulation* (New York: Academic)

[55] Donev A, Torquato S and Stillinger F H 2005 *J. Comput. Phys.* **202** 737–764

[56] Rathore N, Chopra M and de Pablo J J 2005 *J. Chem. Phys.* **122** 024111

[57] Frodl P and Dietrich S 1993 *Phys. Rev. E* **48** 3741

[58] Allen M P and Tildesley D J 1986 *Computer Simulation of Liquids* (Oxford: Clarendon)

[59] Carpency T N, Gunton J D and Rickman J M 2016 *J. Chem. Phys.* **145** 214904

[60] Li Z W, Zhu Y L, Lu Z Y and Sun Z Y 2018 *Soft Matter* **37** 7625–7633

[61] Hatch H W, Mahynski N A, Murphy R P, Blanco M A and Shen V K 2018 *AIP Advances* **8** 095210

[62] Frenkel D, Bladon P, Bolhuis P and Hagen M 1996 *Phys. B* **228** 33–39